Complex Spatiotemporal Evolution of the 2008 Mw 4.9 Mogul Earthquake Swarm (Reno, Nevada): Interplay of Fluid and…

Article *in* Journal of Geophysical Research: Solid Earth · November 2016

DOI: 10.1002/2016JB013399

4 authors, including:

Christine Ruhl
University of California, Berkeley
6 PUBLICATIONS   **7** CITATIONS

SEE PROFILE

Rachel Abercrombie
Boston University
87 PUBLICATIONS   **3,002** CITATIONS

SEE PROFILE

Kenneth D Smith
University of Nevada, Reno
76 PUBLICATIONS   **648** CITATIONS

SEE PROFILE

Some of the authors of this publication are also working on these related projects:

Project   Real-Time GNSS for Earthquake Early Warning View project

RESEARCH ARTICLE

Key Points:
- Mapped complex spatiotemporal seismicity and fault patterns within a well-recorded shallow urban earthquake swarm
- Adapted regional statistical clustering approach to objectively isolate space-time substructures within an individual earthquake sequence
- Identified fault-fracture mesh geometry and seismicity migration rates consistent with pore pressure changes related to fluid flow

Correspondence to:
C. J. Ruhl,
cruhl@berkeley.edu

Complex spatiotemporal evolution of the 2008 *Mw* 4.9 Mogul earthquake swarm (Reno, Nevada): Interplay of fluid and faulting

C. J. Ruhl[1], R. E. Abercrombie[1,2], K. D. Smith[1], and I. Zaliapin[3]

[1]Nevada Seismological Laboratory, University of Nevada, Reno, Nevada, USA, [2]Department of Earth and Environment, Boston University, Boston, Massachusetts, USA, [3]Department of Mathematics and Statistics, University of Nevada, Reno, Nevada, USA

Abstract After approximately 2 months of swarm-like earthquakes in the Mogul neighborhood of west Reno, NV, seismicity rates and event magnitudes increased over several days culminating in an M_w 4.9 dextral strike-slip earthquake on 26 April 2008. Although very shallow, the M_w 4.9 main shock had a different sense of slip than locally mapped dip-slip surface faults. We relocate 7549 earthquakes, calculate 1082 focal mechanisms, and statistically cluster the relocated earthquake catalog to understand the character and interaction of active structures throughout the Mogul, NV earthquake sequence. Rapid temporary instrument deployment provides high-resolution coverage of microseismicity, enabling a detailed analysis of swarm behavior and faulting geometry. Relocations reveal an internally clustered sequence in which foreshocks evolved on multiple structures surrounding the eventual main shock rupture. The relocated seismicity defines a fault-fracture mesh and detailed fault structure from approximately 2–6 km depth on the previously unknown Mogul fault that may be an evolving incipient strike-slip fault zone. The seismicity volume expands before the main shock, consistent with pore pressure diffusion, and the aftershock volume is much larger than is typical for an M_w 4.9 earthquake. We group events into clusters using space-time-magnitude nearest-neighbor distances between events and develop a cluster criterion through randomization of the relocated catalog. Identified clusters are largely main shock-aftershock sequences, without evidence for migration, occurring within the diffuse background seismicity. The migration rate of the largest foreshock cluster and simultaneous background events is consistent with it having triggered, or having been triggered by, an aseismic slip event.

1. Introduction

The Mogul earthquake sequence generated many unusually shallow earthquakes (<6 km depth) that were felt widely in the neighborhoods of west Reno, NV, beginning in late February 2008. In response, the nearby Nevada Seismological Laboratory rapidly installed a total of 13 temporary, telemetered instruments directly above the sequence. Numerous well-recorded events (>7000), including an M_w 4.9 earthquake on 26 April 2008, provide an opportunity to investigate the structure and driving mechanisms of earthquake swarms.

Precisely located microseismicity can be used to examine fault structure, fault evolution and mechanics, and earthquake triggering [*Waldhauser et al.*, 2004; *Valoroso et al.*, 2014; *Ruhl et al.*, 2016]. Direct information about active fault structure and physical properties at seismogenic depths is generally limited to geological studies potentially requiring expensive drilling projects [e.g., *Zoback et al.*, 2010] or studies of exhumed faults [e.g., *Chester et al.*, 1993; *Allen*, 2005]. Other studies have used geophysical techniques such as magnetotelluric and seismic reflection profiles [e.g., *Unsworth et al.*, 1997] and seismic tomography [e.g., *Allam et al.*, 2014] to isolate and study faults at near-surface and seismogenic depths, respectively. Indirect geophysical studies are useful to investigate physical properties of fault zones at broad scales, but often lack the detailed spatial and temporal resolution that precise earthquake locations can provide. Therefore, many studies have used relocated earthquakes to characterize fault zone structure at typical seismogenic depths near major plate boundary faults [e.g., *Waldhauser et al.*, 2004] and in areas of earthquake swarms [e.g., *Pacchiani and Lyon-Caen*, 2010; *Duverger et al.*, 2015].

Earthquake swarms are broadly defined as sequences of earthquakes that cluster in space and time and do not fit a typical main shock-aftershock pattern [*Mogi*, 1963; *Hill*, 1977; *Vidale and Shearer*, 2006]. Swarms are common in areas of volcanic [e.g., *Hill*, 1977] and geothermal activity [e.g., *Waite and Smith*, 2002;

Shelly et al., 2013] and have been associated with driving mechanisms such as aseismic creep [e.g., *Lohman and McGuire*, 2007], magma injection [e.g., *Hill*, 1977], and fluid diffusion [e.g., *Shapiro et al.*, 1997; *Spicak and Horalek*, 2001; *Antonioli et al.*, 2005]. They are most commonly attributed to fluid circulation reducing normal stress via increased pore pressure on preexisting structures, particularly in extensional and transform fault environments [*Vidale and Shearer*, 2006; *Chen et al.*, 2012]. Some authors [e.g., *Hainzl and Fischer*, 2002; *Hainzl*, 2004] have observed the interplay of stress transfer from fluid migration and earthquake-to-earthquake triggering in the evolution of swarm sequences. In addition, *Shimojo et al.* [2014] showed fluid-driven swarm-like sequences initiated by dynamic stress changes related to passing surface waves after the 2011 M 9.0 Tohoku-Oki earthquake. Recent availability of high-quality relocated catalogs allows developing quantitative techniques for discrimination between swarms and main shock-aftershock sequences [e.g., *Zaliapin and Ben-Zion*, 2013b; *Zhang and Shearer*, 2016].

The Mogul sequence provides a high-quality data set to address outstanding questions about both shallow fault structure and spatiotemporal sequence evolution, and their driving mechanisms. We begin by describing the Mogul earthquake swarm and regional tectonic setting. We then develop high-precision waveform-based double-difference relocations and conduct a detailed analysis of fault mechanics and clustering within the sequence using well-constrained focal mechanisms and applying earthquake clustering statistics. We describe the evolution of the sequence and investigate evidence for driving mechanisms including pore pressure diffusion from fluids and aseismic slip.

1.1. The Mogul Earthquake Swarm

Beginning in late February 2008, an earthquake swarm generated many unusually shallow earthquakes (<6 km depth) that were widely felt in the residential Mogul and Somersett neighborhoods of west Reno, NV. This led to significant public concern. Nearly 30 microearthquakes were detected in January and early February 2008 [*Smith et al.*, 2010], while locatable seismicity began on 21–22 February 2008 (largest M_L 0.44; magnitude of completeness for the Reno area is ~0.5). Coincidentally, this was within 1 day of the M_L 6.0 Wells, NV earthquake ~450 km to the east. Numerous felt earthquakes over the next few weeks, increases in activity, and proximity to the Nevada Seismological Laboratory (NSL) at the University of Nevada, Reno, motivated a temporary, telemetered instrument deployment effort as early as 3 March 2008 (Figure 1). Fortuitously, this was several days before the first significant increase in activity, punctuated by an M_L 3.2 earthquake on 8 March 2008 (Figure 2). The *S-P* times of near 0.5 s observed at near-source stations confirmed unusually shallow source depths (<6 km; Figure 3) and explained why even very low magnitude earthquakes (as low as M_L 0.6) were locally felt. Distinct bursts of seismicity grew in spatial extent and intensity over the next 2 months, culminating in the M_w 4.9 main shock at 06:40 26 April 2008 UTC (relocated hypocenter: 39.523 N, 119.922 W, 3.6 km depth). Seismicity rates subsequent to the main shock (Figure 2b) decayed in a similar manner to typical aftershock sequences, following the modified Omori's law [*Utsu*, 1961].

We estimate the Gutenberg-Richter magnitude-frequency b value of the Mogul sequence as 0.94 (Figure 3a), similar to typical main shock-aftershock earthquake sequences. While magmatic and volcanic earthquake swarms are often characterized by high (much greater than 1) b values [e.g., *Sykes*, 1970], low b values (~0.8) have been observed in swarms occurring in the Rio Grande Rift [*Ruhl et al.*, 2010] and in continental rifts worldwide [e.g., *Ibs-von Seht et al.*, 2008].

Previous studies of the Mogul earthquakes have focused on strong shaking produced by the main shock [*Anderson et al.*, 2009], surface deformation recorded by InSAR [*Bell et al.*, 2012], and relocation and ground-truth classification of the largest events [*von Seggern et al.*, 2015]. Double-difference relocations for ~1900 $M_L \geq 1.0$ earthquakes developed by *von Seggern et al.* [2015] align primarily NNW-SSE. Moment tensor solutions for the main shock [e.g., *Smith et al.*, 2008; *Anderson et al.*, 2009] and the aftershock alignments suggest that the M_L 5.1 (M_w 4.9) main shock occurred on a steeply west dipping northwest striking right-lateral fault plane producing ground motions up to 1.1 g [*Anderson et al.*, 2009]. This geometry is observable in the surface deformation measured via InSAR and GPS [*Bell et al.*, 2012]. There is no known fault consistent with the location and orientation of the main shock nodal planes and northwest aftershock alignment; however, it is consistent with local stress orientations [*Ruhl et al.*, 2016]. *Bell et al.* [2012] measured ±3 cm of right-lateral displacement using stacked interferometric pairs from April to August 2008. Two thirds of the measured slip (±2 cm) occurred prior to a 28 May 2008 scene, while ±1 cm of additional slip was recorded by 7 August 2008. *Bell et al.* [2012] found this surface deformation to be equivalent to an M_w 5.3–5.4 event on a shallow
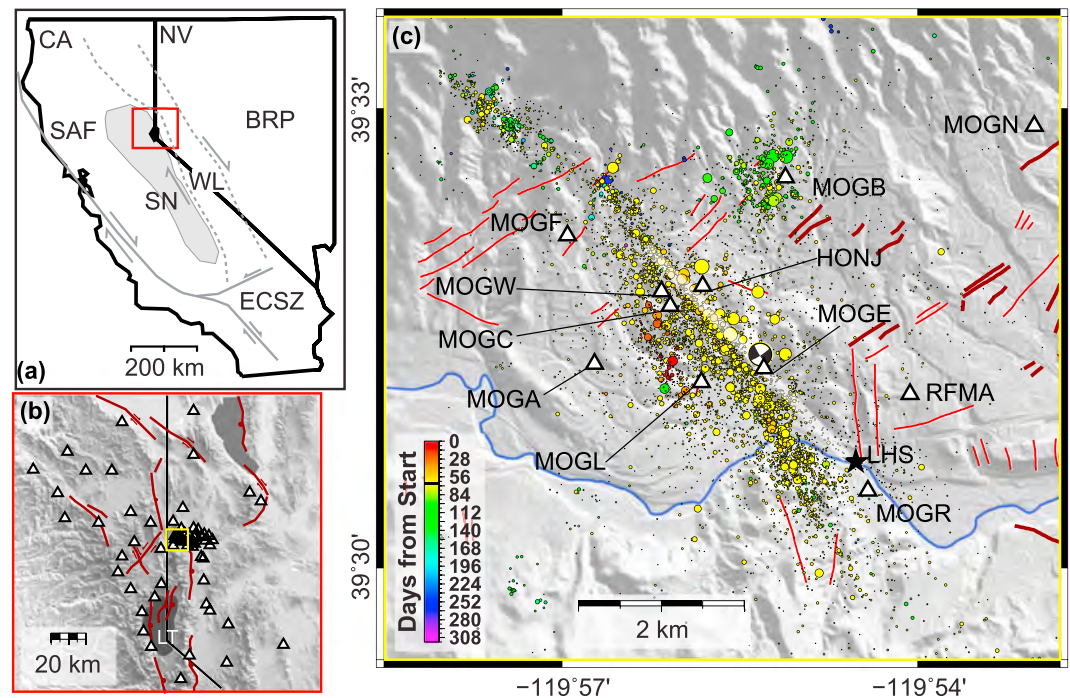
Figure 1. (a) Sketch of tectonic setting of the Walker Lane (WL) in relation to the right-lateral San Andreas fault (SAF) plate boundary system, the stable Sierra Nevada block (SN), and the extensional Basin and Range Province (BRP). The southern WL is also known as the Eastern California shear zone (ECSZ). (b) Regional shaded relief map of Reno area, Lake Tahoe (LT), and seismic stations (triangles) used for relocation. Yellow box shows location of study area. Dark red lines show simplified regional Quaternary faults. (c) Map of relocated earthquakes in the Mogul neighborhood of west Reno, NV sized by magnitude and colored by time in days from 22 February 2008. Black bar denotes time of main shock. Temporary NN seismic stations are shown as white triangles. Quaternary Faults and Folds database shown in light (<1.6 Mya) and dark (<750 Kya) red [*U.S. Geological Survey and Nevada Bureau of Mines and Geology*, 2006]. White line shows location of fault plane modeled by *Bell et al.* [2012] for M_w 4.9 Mogul main shock. Blue curve shows Truckee River and black star shows location of Lawton Hot Springs (LHS).

northwest striking right-lateral fault plane, twice that of the cumulative magnitude of all swarm events greater than M_w 3. This observation indicates significant aseismic slip. Although there were 2 months of foreshocks, preseismic deformation was not detected on InSAR data or in GPS observations [*Bell et al.*, 2012]. However, it is worth noting that the most active phase of foreshock activity occurred within 1 week of the main shock and the timing of the interferometric pairs used cannot constrain slip immediately prior to the main shock [*Bell et al.*, 2012]. In addition, noise in daily GPS solutions could mask up to 4 mm of aseismic slip immediately prior to the main shock (G. Blewitt, personal communication, 2016), which itself had a maximum of only ~9 mm of coseismic offset on station RENO (B. Hammond, personal communication, 2016). The Mogul fault is optimally oriented within Walker Lane principal stresses [e.g., *Ichinose et al.*, 2003; *Ruhl et al.*, 2016] and accommodates shear motion absent in the geologic record [*Wesnousky et al.*, 2012] but seen geodetically [*Hammond and Thatcher*, 2007]. This led *Bell et al.* [2012] to characterize the Mogul sequence as an incipient strike-slip fault in an otherwise local Basin and Range extension-dominated physiography, indicating that the Mogul sequence is part of a westward migration of Walker Lane transtension, at this latitude.

The main shock source depth was extremely shallow, modeled as shallow as 2 km depth from InSAR [e.g., *Bell et al.*, 2012] and near 2.8 km in a previous relocation study of the main shock depth by *von Seggern et al.* [2015]. No surface rupture was identified despite the shallow source depths and observed surface deformation. Discontinuous surface faults (Figure 1) mapped directly above the Mogul swarm cut Tertiary sedimentary and volcanic units and older granites at a variety of orientations over short distances [*Bell and Garside*, 1987]. Local Quaternary faults are also mapped at various orientations to bedrock faults, suggesting a long history of deformation and overprinting of faults in a highly fractured shallow subsurface [*Bell and Garside*, 1987; *Cashman et al.*, 2012]. In addition to being highly fractured, fluids present near Mogul may be associated with
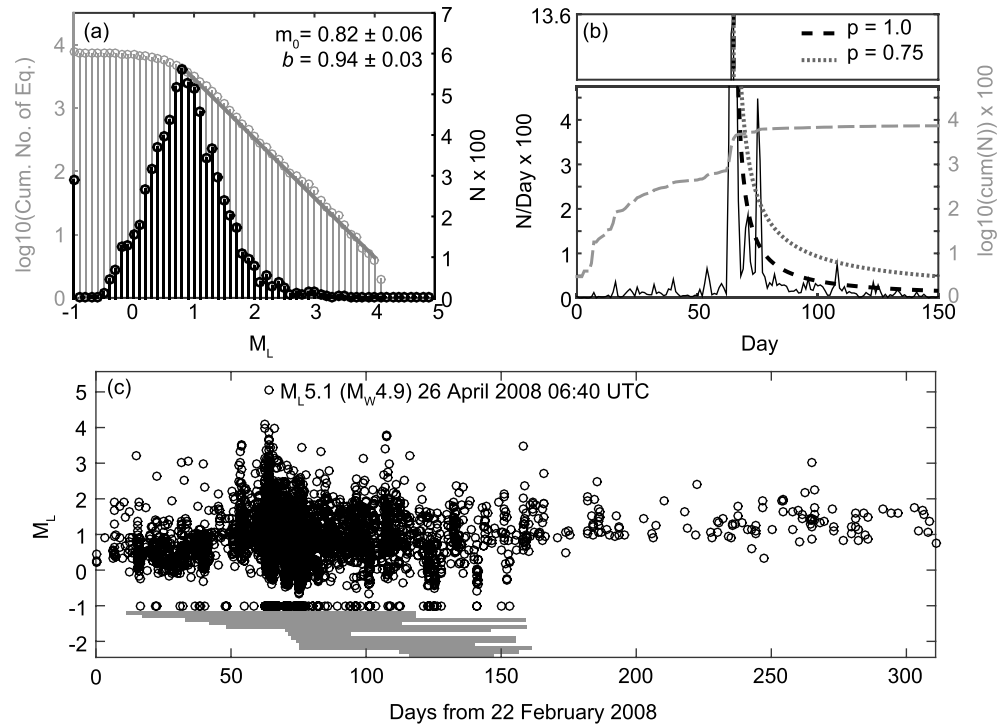
Figure 2. Sequence properties. (a) Cumulative (light gray, left axis) and noncumulative (black, right axis) magnitude-frequency distributions and estimated b value (dark gray line). (b) Earthquake rate per day (black, left axis) and cumulative number of earthquakes (dashed light gray, right axis) for the first 150 days of the Mogul sequence. Predicted aftershock decay according to Omori's law plotted at time of the main shock. (c) Time-magnitude plot of the entire sequence. Main shock is labeled. Horizontal gray lines show installation durations for 13 temporary stations shown in Figure 1.

swarm-like earthquake generation. The Truckee River flows along the southern side of the area of seismicity (Figure 1c). Lawton hot springs, located along the Truckee River, is a granitic sourced hot springs at the southern end of the Mogul earthquake swarm (Figure 1c). Measurements of Lawton hot springs in 1954 suggest a flow rate near 250 gpm with a maximum temperature near 48°C [*Shevenell*, 2016]. A spa facility was operated at the hot springs as early as 1886, but has been out of use for several decades. Measurements of three wells near the hot springs taken on 18 and 22 April, and 2 May 2008 showed no significant change in temperature or flow [*Shevenell*, 2016]. Although no long-term wells were monitored during the sequence, one well in the Mogul neighborhood recorded a ~0.15 m water level rise in response to an M_L 3 earthquake on 30 April 2008 (S. Tyler, personal communication, 2016).

1.2. Tectonic Setting

The Mogul swarm occurred approximately 10 km west of downtown Reno, NV, within the transtensional Walker Lane tectonic province (Figure 1). The Walker Lane is a broad, ~100 km wide zone of discontinuous strike-slip and normal faulting that parallels the San Andreas fault system east of the Sierra Nevada block [*Stewart*, 1988]. It accommodates 20–25% of relative plate motion between the Pacific and North American plates [e.g., *Surpless*, 2008] and GPS models suggest 7–10 mm/yr of right-lateral shear through the Reno area [*Hammond and Thatcher*, 2007]. Despite this measured strain, there is little geologic evidence for through-going right-lateral strike-slip faulting at the latitude of the Reno-Carson City-Lake Tahoe area (Figure 1b), where, in contrast, large westward tilted en echelon normal-fault-bounded range blocks dominate the physiography [*Surpless*, 2008; *Wesnousky et al.*, 2012]. Some investigators consider range-bounding normal faults of the eastern Sierra as an integral part of the Walker Lane, accommodating shear through en echelon extensional geometry and vertical axis rotation [*Wesnousky et al.*, 2012]. Abundant regional seismicity occurs at typical seismogenic depths (approximately 5–17 km); often in the transition zones between and at the terminations of major normal faults [*Ichinose et al.*, 1998; *Ruhl et al.*, 2016]. Most notably in the Reno-Tahoe area, the 1994 northeast striking left-lateral M_L 5.9 Double Springs Flat earthquake occurred between the
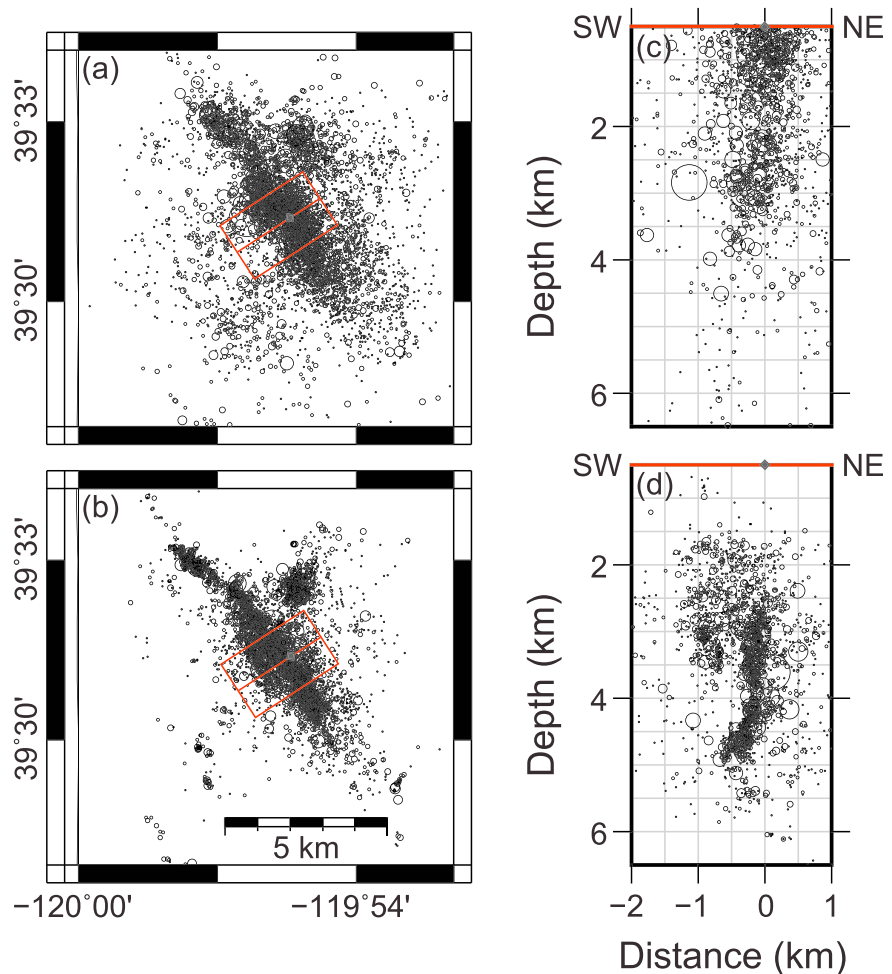
Figure 3. Maps and vertical cross sections of (a, c) 7752 NSL raw catalog hypocenters and (b, d) 7549 double-difference relocated hypocenters for the 2008 swarm, sized by magnitude. Red box on maps show orientation of and events included in cross sections.

Genoa and Antelope Valley normal fault systems about 80 km south of the Mogul sequence [*Ichinose et al.*, 1998]. Historical accounts suggest a long history of moderate earthquakes in the Reno area, in which strong shaking events were often preceded by energetic foreshock periods [*dePolo et al.*, 1997]. Swarms like Mogul emphasize the potential for large or significant earthquakes to occur in areas of evolving microseismicity and the importance of understanding earthquake triggering, even at small scales, particularly in urban areas.

2. Refining the Earthquake Catalog to Resolve Fault Structure

A set of high-quality event relocations and well-constrained focal mechanisms is required to identify active structures and to investigate the evolution of faulting and swarm processes within the Mogul sequence. We begin by building the best absolute location catalog as high-quality input to the waveform-based double-difference relocation technique.

2.1. Data

We use waveforms recorded on 65 NSL (Network Code NN) and Transportable Array (Network Code TA) seismic stations that include a variety of sensors and data logger types, and include temporary stations deployed during the sequence (Figure 1). Source-station distances range from 0 to 100 km and provide good azimuthal coverage. Stations are configured with analog single-component short-period seismometers, digital three-component broadband and short-period sensors, and digital three-component urban accelerometers that

Table 1. Homogeneous Layered Velocity Model Used for Earthquake Relocation

Depth (km) to Top of Layer	P Wave Velocity (km/s)
0.0	3.5
1.0	4.5
2.0	5.5
4.0	6.0
7.0	6.4
18.0	6.8
38.0	7.0
50.0	7.5

were in operation during part or all of the sequence (Figure 1 Inset). Station sampling rates range from 40 to 200 Hz. In total, 13 temporary IRIS RAMP systems, integrated within the NSL regional microwave network for real-time data acquisition and processing, and configured with broadband sensors and accelerometers, were deployed in a 10×10 km area directly above the sequence (Figure 1). NSL detected over 15,000 earthquakes in the Mogul area over the duration of temporary station deployment (detection threshold < -0.5 M_L). Additional very small events may be identified from continuous waveform records but are generally not locatable with confidence (all data from permanent and temporary stations are available from the IRIS Data Management Center, http://www.iris.edu).

2.2. Absolute Earthquake Relocation

We select 7752 earthquakes (Figure 3a) with a minimum of 10 defining phases from the NSL Datascope database for initial absolute location using USGS program *HYPOINVERSE* [*Klein*, 1978]. The remaining events (~7000) are generally small magnitude, with too few phases for high-precision relocation. We use the same velocity model as *von Seggern et al*. [2015], shown in Table 1. Because of the shallow character of the sequence in an area of high relief, we apply station elevation corrections assuming a 3.5 km/s velocity to adjust arrival times to the mean-station elevation of 1.73 km, similar to elevations in the Mogul neighborhood. To account for variations from the local 1-D velocity model, we reran the location routine adjusting arrival times at each well-recorded station by the average travel time residual for arrivals at that station. Median corrections are 0.03 s and 0.05 s for *P* and *S* waves, respectively. Resulting station residuals, as well as overall location uncertainty, decrease with this approach. The density and geometry of near-source stations result in 85% of events having absolute vertical and horizontal location uncertainties less than 1.2 and 2.0 km, respectively.

2.3. Double-Difference Relocation With Cross Correlation

To improve relative location precision, we use the double-difference relocation program *HypoDD* [*Waldhauser and Ellsworth*, 2000] to pair each earthquake with up to 30 of its nearest neighbors within 2 km hypocentral distance based on the adjusted HYPOINVERSE output. Each pair may have up to 25 linked phase arrivals. These parameters result in 145,478 linked event pairs with an average of 10 links per pair, a mean distance of 0.4 km, and a total of 1.57 million catalog arrival time pairs.

Phase pairs are then cross correlated using a 0.5 s and 1.0 s window around the *P* wave and *S* wave arrival times, respectively. After initial adjustment of event pairs with correlation coefficients greater than 0.6, we resample the time series over a 0.1 s and 0.2 s window to 4 times the initial sample rate and adjust relative waveform positions to maximize the cross-correlation coefficient for *P* wave and *S* wave arrivals, respectively. The subsample lag times are used to refine the differential times for 974,830 individual waveform pairs. Both catalog and cross-correlated differential times are used to optimize interevent distances, totaling 2.55 million differential times. Earthquakes that locate above the surface or lose connection to other events are dropped during the HypoDD inversion. This resulted in a loss of 203 events (2.6%) and a final count of 7549 relocated earthquakes (Figures 1 and 2). While absolute location errors are around 1–2 km, location uncertainties from singular value decomposition analysis on 775 events in 69 small clusters (see section 3 for clustering details) have median uncertainties in all three directions of 35 m and a mean of 70 m, with 85% of events having hypocentral errors less than 90 m. We assign 100 m as a conservative overall relative location uncertainty to all earthquakes in the relocated set (Figure 2b). The geometry of the resulting relocations is very similar to that of *von Seggern et al*. [2015], but with the addition of over 5000 events (totaling ~4 times as many events).

2.4. Focal Mechanisms

We compute double-couple earthquake focal mechanisms from *P* wave polarities using USGS program *HASH* [*Hardebeck and Shearer*, 2002]. We find 1082 well-constrained focal mechanism solutions (M_L 0–4.14) using the

following selection criteria: at least 10 first motions with fault plane uncertainties, azimuthal gaps, and takeoff angle gaps of no more than 35°, 90°, and 45°, respectively (Figure S1 and Data Set S1 in the supporting information). Additionally, we determine regional surface wave moment tensors for the 11 largest events (M_w 3.2–4.9) from a set of trial solutions based on an assessment of the percent double couple and variance reduction between synthetic and filtered waveforms [e.g., *Ichinose et al.*, 2003]. The double-couple first-motion mechanisms for these events match the moment tensor results within the HASH fault plane uncertainties.

2.5. Initial Observations of Fault Structure

Earthquake relocations provide a basis to characterize detailed fault structure within the Mogul earthquake swarm (Figure 3). Foreshock activity is offset to the west from the main shock and aftershock seismicity alignments (Figure 1c). Earthquakes in the main northwest trending zone define a narrow region of subparallel, subvertical dextral strike-slip faults that begin to dip west at around 4 km depth (Figure 3), possibly to accommodate normal motion at several locations at those depths. In addition to a change of fault dip and sense of slip with depth, we see variations in fault strike. North of the main shock, seismicity-oriented N44°W aligns with the fault plane modeled by *Bell et al.* [2012], whereas south of the main shock, relocated activity diverges from the InSAR modeled fault plane (Figure 1c), trending more northerly. The geometry indicates a kinked (or curved) fault plane in which the main shock initiated near the vertex of both vertical (dip) and horizontal (strike) change. Relocations and focal mechanisms for the main shock and immediate aftershocks suggest primarily right-lateral strike-slip motion. Despite being curvilinear, the main fault zone remains narrow (<1 km) from ~5.5 km to ~3 km depth. Above 3 km depth, seismicity is more broadly distributed. This apparent broadening or scattering of the shallowest activity may be an artifact of velocity model error and/or increased velocity heterogeneity at such shallow depths; however, uncertainties do not systematically increase. Nonetheless, including the off-fault foreshock seismicity in the fault zone width estimate indicates an NE-SW widening of active structures approaching the surface from ~0.25 km width at 5.5 km depth to ~1.25 km width at 2 km depth.

The fault geometry at Mogul is similar to observed [e.g., *Allam et al.*, 2014] and theoretical damage zones in developing strike-slip faults at shallow depths [*Finzi et al.*, 2009] as well as fault structure in major strike-slip faults [e.g., *Schaff et al.*, 2002]. *Finzi et al.* [2009] found that low-velocity damage zones form before as much as 50 m of offset has been accumulated on evolving fault systems. Studies of exhumed strike-slip faults, including abandoned branches of the San Andreas fault [e.g., *Chester et al.*, 1993] and pseudotachylyte systems in the Rocky Mountains [e.g., *Allen*, 2005], indicate multiple parallel planes in the fault zone, similar to what we observe in the seismicity in the Mogul sequence. The similarity in observations may support the hypothesis that the Mogul fault is an incipient fault structure within the northwestward evolving Walker Lane.

3. Statistical Cluster Analysis

The relocated catalog is highly clustered in space and time (Figures 1c and 3d). To investigate spatial and temporal features of seismicity, events should be grouped in relation to individual active structures. Manually identifying earthquakes associated with structures is laborious, slow, and subjective; therefore, we introduce below an automatic method to identify dependent event clusters within the swarm. We approached this by extending the general cluster method of *Zaliapin et al.* [2008].

3.1. Method to Subdivide Sequence

Following *Zaliapin et al.* [2008] and *Zaliapin and Ben-Zion* [2013a], we compute the space-time-magnitude proximity between an earthquake *j* and *an earlier earthquake i*:

$$n_{ij} = \tau_{ij} r_{ij}^{d_f} 10^{-b(m_i - m_0)} \quad for \quad \tau_{ij} \geq 0, \tag{1}$$

where $\tau_{ij} = t_j - t_i$ is the interevent time, r_{ij} is the hypocentral separation, *b* is the Gutenberg-Richter frequency-magnitude *b* value, m_0 is the magnitude of completeness, and d_f is the fractal dimension of the hypocenters. Using ZMAP [*Wiemer*, 2001], we calculate the maximum likelihood estimates of the magnitude of completeness, *b* value, and fractal dimension as 0.82 ± 0.06, 0.94 ± 0.03, and 2.3 ± 0.001, respectively (Figure 2). Previous studies suggest that overall cluster structure is insensitive to the lower magnitude limit [e.g., *Zaliapin and Ben-Zion*, 2013a]; specifically, considering events below the completeness magnitude has almost no effect on the

distribution of the distance (1), the total number of detected clusters, and assigning earthquakes to individual clusters (see related definitions below). Accordingly, to include as many events as possible, we use the minimum event magnitude (−0.75) rather than the magnitude of completeness. We experimented with different values of the minimum examined magnitude and found that general cluster geometries and relationships are unaffected by this parameter. In contrast to *Zaliapin et al.* [2008] we use hypocentral rather than epicentral distances; this is possible because vertical location uncertainties in the examined data set, in contrast to most catalogs, are less than horizontal uncertainties. This is due to the dense geometry of stations in the source area and the fact that many small events are only recorded on near-source stations directly above the swarm. Shallow events recorded only on near-source stations will be well constrained both horizontally and vertically, while a deeper event recorded only on near-source stations will have equally small vertical uncertainties but increasing horizontal uncertainties with depth as the aperture of horizontal coverage narrows.

Cluster identification is done using the distance of equation (1). Specifically, for every earthquake *j* in the catalog, we find its nearest neighbor *i* according to the distance (1). The event *i* is called the parent of *j*; and the event *j* is called an offspring of *i*. The respective nearest-neighbor distance is also denoted by n_{ij}, which does not create confusion with the general distance notation used in equation (1). The nearest-neighbor distance n_{ij} has a prominently bimodal distribution in the observed catalogs and cluster models [see, e.g., *Zaliapin and Ben-Zion*, 2013a]. The high-distance mode corresponds to background events, similar to those observed in a (possible space-inhomogeneous) Poisson process, and the low-distance mode corresponds to clustered events (events that happened much closer to their parents than is expected in a Poisson process). We refer to *Zaliapin and Ben-Zion* [2013a] for further discussion and examples.

The nearest-neighbor parent-offspring links connect all earthquakes in the examined catalog in a single-spanning network. Removing the long links—those with nearest-neighbor distance above a threshold ($n_{ij} > c$)—partitions this network into multiple subnetworks; or, equivalently, this partitions the catalog into individual clusters connected by short links ($n_{ij} < c$). Clusters that consist of a single event (that is earthquakes with no close parent and no close offspring) are called singles; the other clusters are called families.

We also define the rescaled time and distance components of the nearest-neighbor distance as follows:

$$T_{ij} = \tau_{ij}10^{-qb(m_i - m_0)}, R_{ij} = r_{ij}^{d_f}10^{-pb(m_i - m_0)}, p + q = 1. \tag{2}$$

This definition ensures that $\log_{10}n_{ij} = \log_{10}T_{ij} + \log_{10}R_{ij}$, which is convenient for interpretation and visualization of the results, as well as for better depicting the bimodality of the nearest-neighbor distance (e.g., see Figure 4 below). The clustering threshold *c* is visualized as a line that separates the bimodal distribution of background and clustered seismicity (e.g., Figure 4a).

We start by applying this method to the 2000–2015 NSL Catalog for the state of Nevada for comparison. The catalog consists of 3271 events with $M_L \geq 3.0$. The large regional catalog has a bimodal distribution of the nearest-neighbor distances (Figure 4a), representing background and clustered seismicity populations similar to previous regional studies [e.g., *Zaliapin and Ben-Zion*, 2013a]. A cluster threshold *c* (solid line in Figure 4a) can easily be chosen to separate the two modes of the bimodal distribution. The Mogul sequence, however, is highly clustered without an apparent bimodal pattern (Figure 4b). In the scope of a larger catalog (e.g., all of Nevada, Figure 4a) the Mogul sequence would be identified as a single cluster using the regionally based threshold of $10^{-4.5}$. Despite the unimodal character of the nearest-neighbor distance distribution shown in Figure 4b, it is obvious from examining a map of locations of the sequence colored by time (Figure 1c) that the Mogul cluster itself is in fact comprised of spatiotemporal subclusters. Because the thresholds in the earlier applications of this clustering approach are chosen to separate the random and clustered earthquake populations, and because Mogul only has one of those (i.e., clustered), we need a new approach to find an appropriate clustering threshold for a finer partitioning of this sequence. This is done by a resampling approach as described below.

We create a synthetic population of unclustered events by reshuffling the times and magnitudes of the Mogul catalog 50 times. The result is a catalog of 377,450 reshuffled events (Figure 4c) that has the same time and space marginal distributions as the examined catalog, but lacks any space-time-magnitude correlations among the events. If one selects a threshold that bounds this distribution from below (dashed line in Figure 4c), then any pair of events that is closer in space and time than this threshold can be considered clustered (i.e., statistically dependent). For Mogul, we use a threshold of $10^{-7.5}$, which removes 87% of events from the randomized catalog (Figure 4c). Zooming into the foreshock time period only (Figure 4d), it is
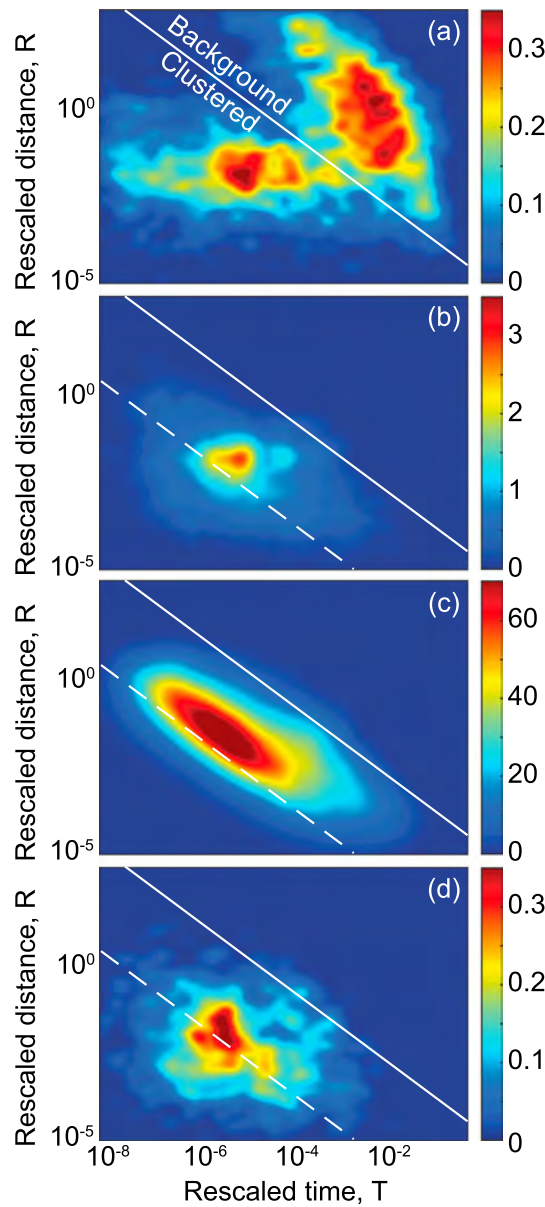
Figure 4. Joint distributions of the rescaled time and space components of the nearest-neighbor earthquake distance. (a) Nevada earthquakes during 2000–2015 (3271 events), (b) double-difference relocations for entire Mogul swarm (7549 events), (c) reshuffled Mogul catalog (377,450 events), and (d) Mogul foreshock period up to the main shock (1408 events). Solid lines show approximate bimodal threshold (−4.5) that separates clustered (below the line) and background (above the line) events in the Nevada catalog; dashed lines denote clustering threshold of −7.5 used in this study. Color scales represent number of events; values vary with the size and nearest-neighbor distributions of each catalog.

obvious that some events are especially highly clustered and do, in fact, lie below this threshold chosen from the reshuffled catalog. This value results in subclusters that most closely match those chosen by hand previously. We find the clustering results to be robust with thresholds within 10^{-7}–10^{-8}. Using thresholds outside of this range may result in unwanted grouping of distinctly different structures and/or a larger number of small, uninteresting clusters.

3.2. Clustering Results

Our new application of the statistical clustering method quantitatively and efficiently clusters events within the Mogul earthquake sequence that were previously grouped through subjective manual inspection of timing, locations, and focal mechanisms from initial observations. We compare our clusters to those picked previously by hand and find that it does a good job of isolating groups clearly related to individual structures. We begin by describing general results of the statistical clustering analysis including pitfalls of the method (Figure 5). We then describe the spatial and temporal characteristics of nonclustered (background) and clustered earthquakes (Figures 6–9).

Our analysis results in 527 clusters of two or more events (39% of relocated earthquakes) and 4603 independent events (singles or clusters of one, 61%). Distributions of cluster sizes and durations are shown in Figure 5, although meaningful interpretation is limited by using the minimum magnitude rather than the actual magnitude of completeness. We focus on the 103 clusters that have either five or more events or a main shock of M_w 2.5 or greater; those clusters represent 26% of all the events and 66% of the clustered events. We refer to these 103 subclusters in subsequent discussion and figures by cluster number (e.g., C1, C2) in chronological order. Earthquakes in smaller clusters and clusters of one are referred to as "background events" throughout this paper. It is important to note that our focus is on detecting the most significant cluster structures, and hence, our so-called background events are not equivalent to background seismicity resulting from typical declustering methods.
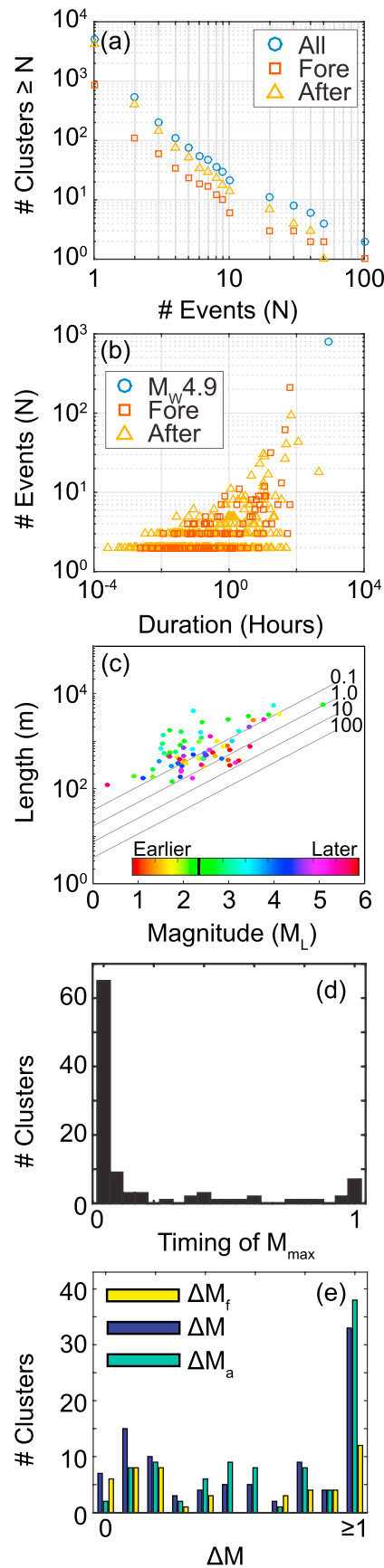
Figure 5a shows that the distribution of cluster sizes approximately follows a power law, similar to the results presented by *Anderson and Nanjo* [2013] for larger catalogs in Nevada and Japan, and by *Zaliapin and Ben Zion* [2013a] and *Gu et al.* [2013] for southern California. The M_w 4.9 main shock cluster is the largest cluster comprising 10.5% of all earthquakes (798 events; Figure 5a). Foreshock clusters, with main shocks before the time of the M_w 4.9 earthquake, comprise 28.1% of clusters representing 18.8% of total events, while aftershock clusters consist of 70.8% of clusters and 70.7% of all events. Clusters are generally quick activations with short durations (Figure 5b) and no clear migration (Figure S2). We estimate the relative timing of the largest event by normalizing its position within each cluster by the cluster duration (Figure 5d). The majority of clusters appear to be main shock-aftershock sequences, with maximum magnitudes at or near the start of each group. Figure 5e shows that most clusters also have a distinct main shock; the average magnitude difference between the largest and second largest earthquakes is 0.8 magnitude units.

To check that this is not a direct consequence of using a clustering method that is magnitude dependent, we rerun the clustering analysis

---

Figure 5. (a) Distribution of cluster size *N*. (b) Cluster duration versus cluster size (*N*) for all clusters. (c) Maximum cluster magnitude versus cluster length estimated using principal components colored by cluster initiation time. Black bar denotes time of main shock. Lines of constant stress drop are calculated assuming a simple, circular source model: $R^3 = 7/16\, M_0/\Delta\sigma$ [*Eshelby*, 1957]. (d) Histogram of duration-normalized main shock timing within each cluster for 103 clusters of interest. (e) Histogram of magnitude difference between each cluster main shock and its largest foreshock (ΔM_f), the second largest event (ΔM), and its largest aftershock (ΔM_a).
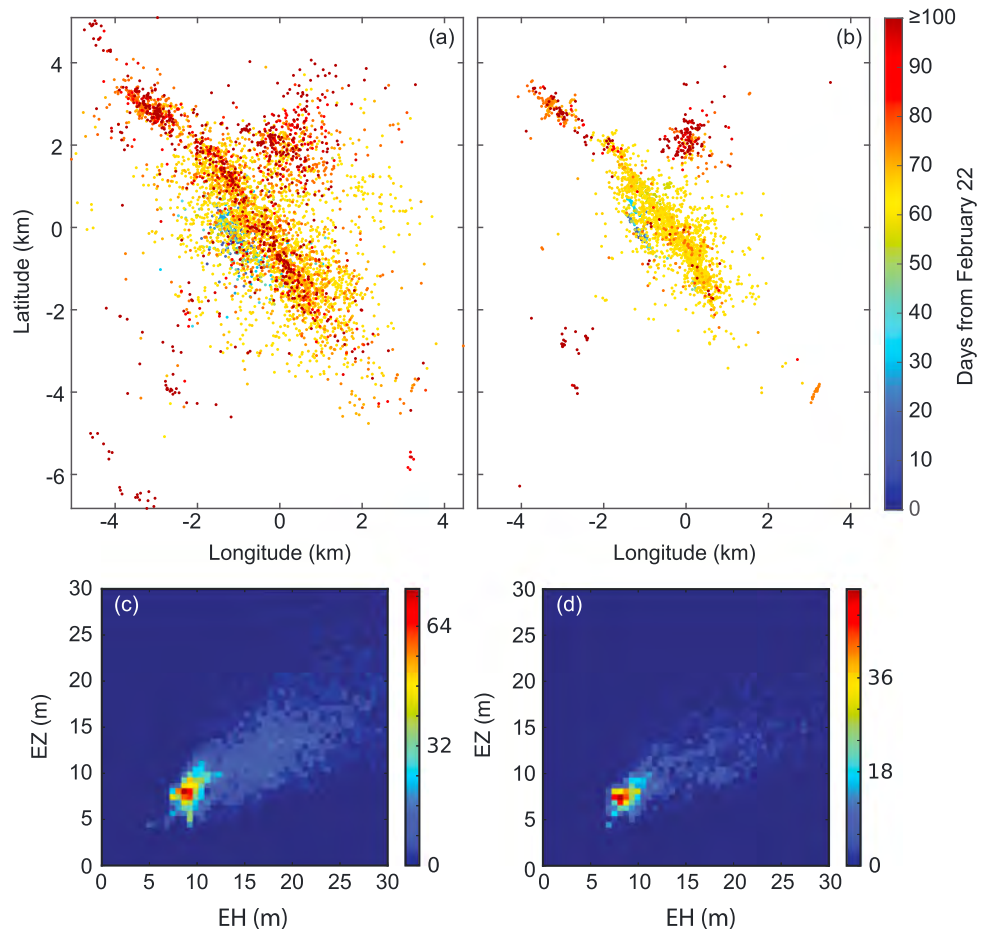
Figure 6. (a) Background events colored by time. (b) Clustered events colored by time. (c) Two-dimensional histrograms of relative background (d) and clustered earthquake location uncertainties from HypoDD.

with a *b* value of zero in equation (1), which is equivalent to assuming that all events have the same magnitude. The resulting clusters are either similar in size and duration or are broken into many smaller clusters that together make up a group similar to the magnitude-dependent clusters. We also attempt to cluster a reshuffled catalog to ensure that temporal features are not an artifact of the method. We find through visual inspection that our results are robust within a range of parameters near our preferred values of b, d_f, m_0, and c. Resulting clusters match what is visually obvious in the relocations and similar focal mechanisms within clusters confirm that our approach is physically valid.

We estimate the length of each cluster of interest with five or more events using principal components. The first principal component of the seismicity point cloud, in other words the longest axis of the seismicity cluster, is used as the length (Figure 5c). Cluster lengths generally scale with magnitude, although clusters around the time of the M_w 4.9 main shock (greens/teals) appear to extend farther than foreshock and distant aftershock clusters of similar magnitudes. This is not surprising, as earthquake-to-earthquake triggering and overall seismicity rates are expected to be higher in the immediate aftershock period of a large event.

3.3. Pitfalls of Clustering Method

The statistical clustering method proved successful at isolating structural and temporal features, but there are several pitfalls to our method to be aware of. First, detailed analysis requires hypocentral rather than epicentral distance. The same approach using only epicentral distances results in many fewer clusters with many more events per cluster, smearing the spatiotemporal details that we aim to isolate. High-quality depths are thus required. Second, some features that we would manually identify and isolate could not be satisfactorily separated using the space-time-magnitude distances with any set of parameters. For example,
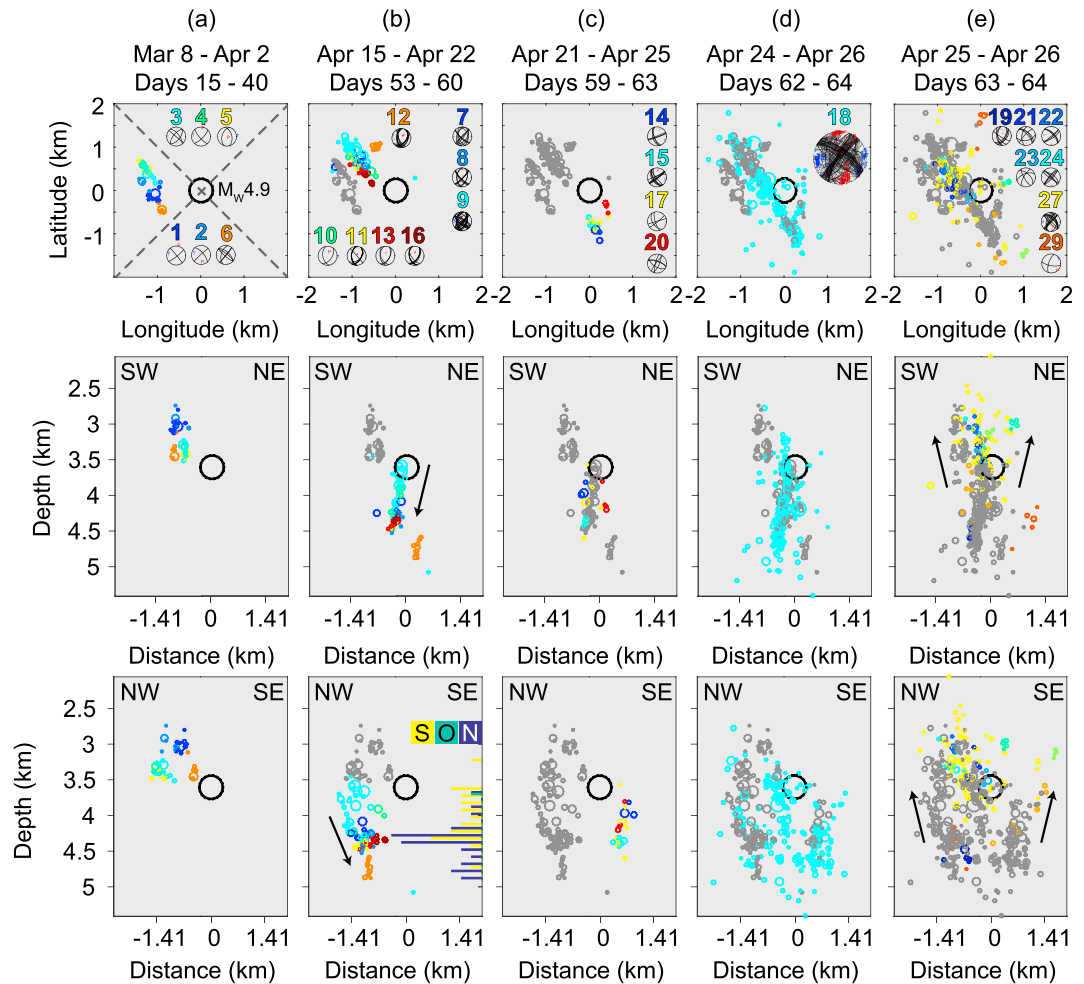
Figure 7. (top row) Maps, (middle row) vertical fault-perpendicular, and (bottom row) longitudinal cross sections of fore-shock cluster events. All cross sections are the same as those shown by dashed lines in Figure 7a with views oriented N45°W (Figure 7, middle row) and N45°E (Figure 7, bottom row). Gray events are those from previous time frames, which are labeled at top. Black circle is hypocenter of M_w 4.9 main shock (C30) on 26 April 2008. Numbers indicate cluster index for each set of focal mechanism solutions shown. Black arrows denote interpreted migration patterns. Horizontal histogram in Figure 7b shows distribution of faulting type with depth where N, O, and S are normal, obliquely normal, and strike-slip mechanisms, respectively.

time-inseparable clusters (e.g., C18, Figures 7d and 9d) have multiple spatial structures (e.g., conjugate faults) that rupture simultaneously or near-simultaneously so that they cannot be separated. Space-inseparable clusters (e.g., C79, Figure 8c and 9f) occur on the same fault patch, but are separated by insufficient time to be effectively declustered. Third, because of the incomplete catalog, some small magnitude yet coherent spatiotemporal features are lost due to insufficient numbers of events (<5) within a statistically significant cluster. A general review of the possible artifacts of the cluster analysis with respect to various catalog uncertainties is given by *Zaliapin and Ben-Zion* [2015].

3.4. Characteristics of Background Events

We define background events as all earthquakes in clusters with less than five total events and with maximum magnitudes of less than 2.5. The background earthquakes shown in Figure 6, and discussed here, include both statistically independent events (4603 clusters of one) and clusters too small to be meaningfully analyzed (1007 events in 420 clusters of <5 earthquakes). Background earthquakes occur diffusely through space and time (Figures 6 and 9a), while clusters, as expected, appear tightly grouped both spatially and temporally (Figures 7–9). This scatter is not a result of increased absolute or relative location uncertainty

for background earthquakes. Although not visible in the space-time-magnitude histogram of the entire Mogul cluster (Figure 4b), the distinct separation between a background population and spatiotemporal clusters can be seen using the foreshock catalog alone (Figure 4d). Background activity spreads at faster rates than foreshock clusters and without well-defined geometric alignments (Figure 6a).

4. Spatiotemporal Evolution of the Mogul Earthquake Swarm

We use statistical clusters and focal mechanisms to describe and constrain the complex spatiotemporal and kinematic evolution of the Mogul swarm. We begin by discussing foreshock clusters in five chronological spatiotemporal groups (Figure 7), before describing features of the main shock and aftershock clusters in spatial groups (Figure 8).

4.1. Spatiotemporal Evolution of Foreshock Clusters

After approximately 2 weeks of diffuse background seismicity, six clusters occur in four distinct bursts from 8 March to 2 April (Figure 9a). These are shown in map view in Figure 7a (top row), and in vertical cross-section view looking N45°W (Figure 7a, middle row) and N45°E (Figure 7b, bottom row). The M_w 4.9 main shock is included in each plot for reference. Focal mechanisms and seismicity alignments indicate that these clusters occurred on two closely spaced, roughly parallel northwest striking planes with right-lateral strike-slip and normal-oblique slip (Figure 7a). Clusters migrate to the northwest along a northwest trend (C1 and C2, blue) and then migrate onto the parallel structure offset to the northeast by approximately 200 m (C3–C5, green). Depths range from approximately 2.5 to 3.5 km, evolving deeper with time from blue to red. Activity concentrates on the second lineament before extending the first farther to the southeast (C6, red). The clusters themselves comprise a small percentage of total events during that time period (14%). Background earthquakes before and during this time are diffuse and cover a distance 2–3 times the dimension of the clusters themselves (Figure 9a).

The next intense burst of activity occurs 2 weeks after C6 ends at depths between 3.5 and 5 km (Figure 7b). In Figure 7 (column b) previous clusters are plotted in grey to show relative motion. Again, clusters are colored blue to red with time. Seven of the eight identified clusters in this time period (Figure 7b) occur on a third subparallel northwest striking structure offset to the northeast of the first month of foreshock clusters. These clusters occur on and begin to define the eventual fault plane of the M_w 4.9 main shock rupture. It dips steeply to the west and focal mechanisms of clusters are both strike-slip (shallow) and normal (deeper) with an abrupt change near 4 km (Figure 7b, bottom row). The clusters migrate downward with time, similar to the first group as indicated by color progression and the arrows in cross section. C12 (orange) occurs on an isolated, slightly deeper roughly north striking normal fault northeast of (Figure 7b, top row) and deeper (Figure 7b, middle row) than the main structure.

The third group of seismicity (Figure 7c) includes four clusters and extends the northwest striking lineament from the previous week farther southeast, leaving a ~1 km gap in between the two active areas. Depths are similar to the second group of clusters, again shown in grey to compare, and vertical cross section (Figure 7c, middle row) indicates that it is aligned with the plane defined by the second group (Figure 7b). Cluster C20 (red) is likely a northeast striking conjugate fault, although fewer numbers of events limit more detailed characterization. It is overlain by a clear conjugate structure that is part of the cluster (Figure 7d).

C18 is the largest foreshock cluster (213 events; Figure 7d) and includes two of the largest foreshock events (M_w 4.11, M_w 3.98). These two cluster "main shocks" occur within 8 min of each other on 24 April 2008, approximately 32 h before the M_w 4.9 main shock. C18 extends the distribution of earthquakes in the Mogul swarm approximately 3 km NW-SE and ~2 km in depth (Figure 7d). It connects groups two (Figure 7 b) and three (Figure 7c) in map view and extends the plane vertically in both directions. It also triggers events on and near previous cluster structures and includes a time-inseparable conjugate structure (Figure 7d) extending northeast from near the southeastern end of clustered seismicity, and initiating near the area of the third burst in Figure 7c (C20). Interestingly, the fault patch that ruptured in the weeklong second burst (C7–C9, blue/green in Figure 7b) does not host additional seismicity throughout the foreshock sequence.

Following C18, seismicity migrates back to more shallow depths as indicated by the arrows in Figure 7e (bottom row). Several smaller foreshock clusters occur within 1 day of the main shock in the volume above C18 (2.5–4.0 km), although many events are concentrated in "gaps" observed on the main shock fault plane.
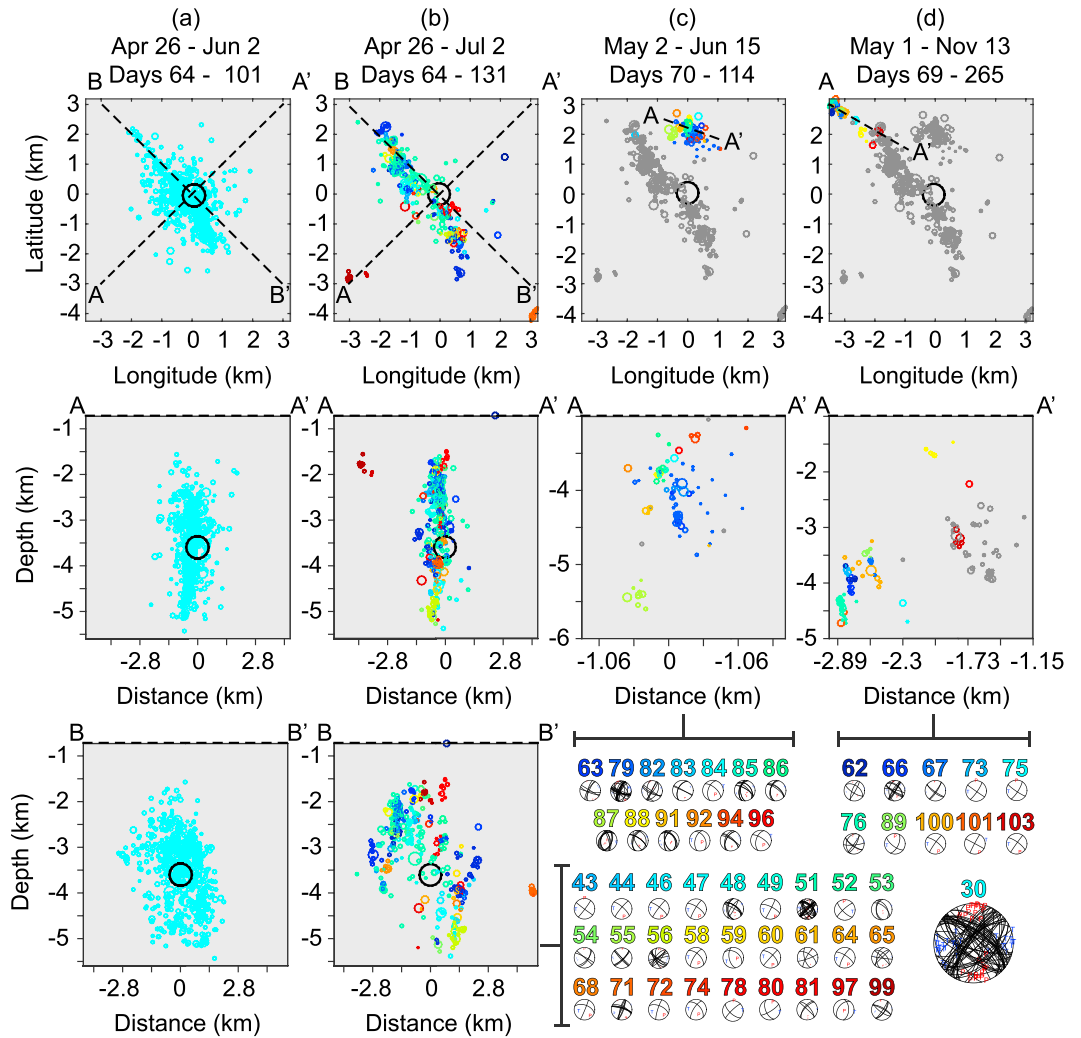
Figure 8. Spatiotemporal plots of (a) the main shock and (b) the near-fault aftershock clusters organized the same as Figure 7. (c, d) Off-fault aftershock clusters with cross sections (second row) oriented as shown by lines A-A' on each map (top row). See Figure 7 caption for specifics. Brackets denote corresponding focal mechanisms for each panel, shown at bottom right and colored by cluster timing as explained in the text.

Focal mechanisms include both strike-slip and normal faulting events during this period. More information about the migration patterns and timing of background events following C18 and upward migration of clusters C19 through C29 are shown in Figure S3.

4.2. Characteristics of Aftershock Clusters

The M_w 4.9 main shock and aftershock clusters are shown in map and cross-section views in Figure 8. Panels are set up similarly to Figure 7. The main shock cluster (C30) includes 798 events, many of which are triggered events on previous cluster structures or within the diffuse volume of seismicity (light blue seismicity in Figure 8a and the many mechanisms labeled "30" in the bottom right of the figure). Depths range from 1.5 to 5.5 km and the width of the seismicity zone widens upward from ~0.5 km width at 5.5 km depth to 2.5 km width at 1.5 km depth. Aftershocks associated with the main shock occur chaotically on and around the fault zone (Figure 8a). The spatial extent of events within cluster C30 (Figure 9e) is generally consistent with the dimension predicted assuming a simple, circular rupture with a stress drop of 3 MPa [*Eshelby*, 1957].

The remaining aftershock clusters (C31–C103) are broken out spatially into three groups: near-fault aftershocks (Figure 8b), northeast aftershocks (Figure 8c), and northwest aftershocks (Figure 8d). Both the relocations and focal mechanisms (labeled, where available) suggest that the near-fault aftershocks occur
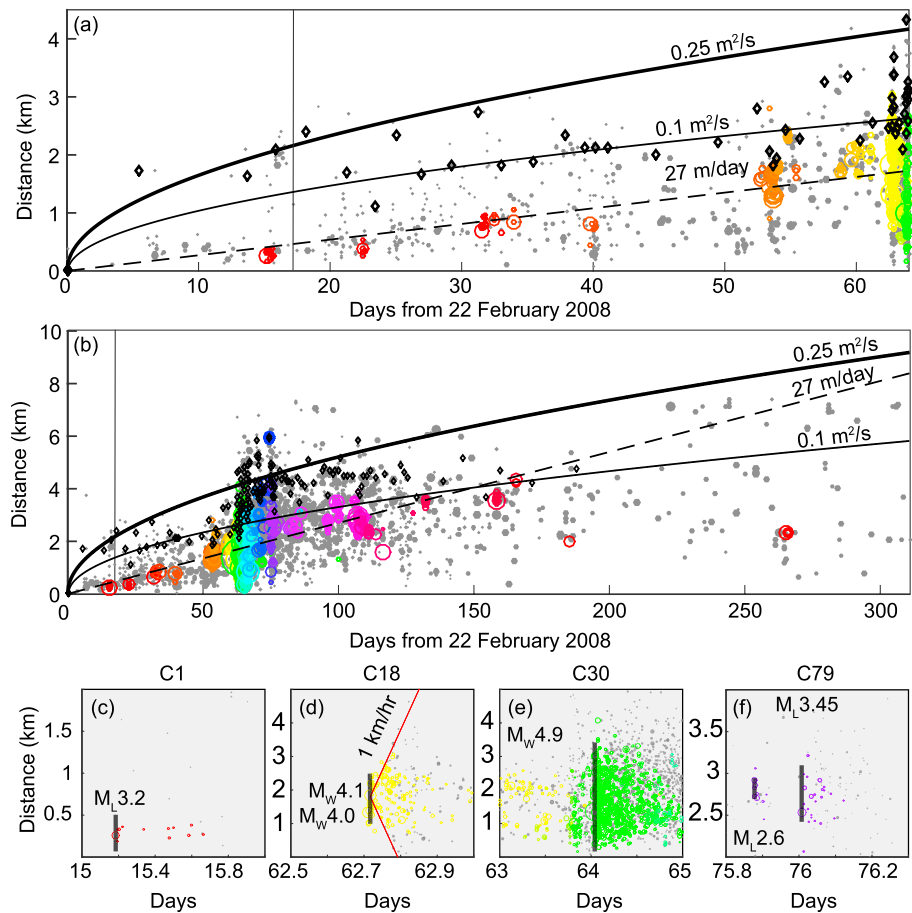
Figure 9. Hypocentral separation of events with time since first event for (a) foreshock period and (b) the entire sequence. Thick and thin black curves show diffusion rates of 0.25 m^2/s and 0.1 m^2/s, respectively. Dashed line is a constant migration velocity of 27 m/d. Black diamonds show the distance at which 95% of events are below, done using 25-event windows. Gray circles are background events and colored circles are earthquakes in identified clusters. Thin vertical line shows time at which two temporary stations were installed. In Figures 9c through 9f the gray lines show lengths of ruptures predicted by assuming a stress drop of 3 MPa using the magnitudes shown. (c) Cluster C1 shows an example of an impulsive foreshock cluster that starts with the largest earthquakes. There are also distant background events seen during this time. (d) Cluster C18 and nearby background events. Red lines show migration velocity of 1 km/h starting from the time and location of the C18 main shock and extending in both directions. (e) Cluster C30, the M_w 4.9 main shock cluster, which reaches its full extent at initiation. (f) An example of an inseparable aftershock cluster, C79, composed of two fast activations on the same structure separated by only a few hours.

on a complex distribution of activity and structures parallel, perpendicular, and conjugate to the main shock fault plane and within a narrow zone (~0.5–1.0 km). The fault-parallel cross section of near-fault aftershocks reveals vertical streaks along the fault plane, potentially indicative of a corrugated or coalescing fault plane or intersecting joints (Figure 8b, B-B′). The seismicity streaks have an average width of ~400 m equivalent to a wavelength of ~800 m. Horizontal motion on a surface with vertical corrugated geometry would produce locked ridges and opening troughs. Ridge asperities would be more likely to produce earthquakes represented by the aftershock streaks (Figure 8b). The fault dip increases with depth, defining a kinked or curved fault plane. Curved and corrugated fault geometries are typical of dip-slip faults and could be evidence of reactivation or reorganization of an older structure or structures. Or, perhaps, this is a small-scale feature of developing strike-slip fault zones. Understanding fault zone geometry is essential to understanding how faults evolve and the mechanics of earthquake rupture.

The northeast group of aftershocks (Figure 8c) initiates 1 week after the main shock. In terms of magnitudes, it is the most energetic area for aftershock generation occurring on well-defined vertical strike-slip and northwest dipping oblique and normal structures. Many of these structures strike northeast and are consistent

with the strike, but not necessarily the dip and sense of slip of Quaternary normal faults shown in Figure 1c. Instead, Mogul structures tend to dip to the northwest. An additional zone of aftershocks initiates northwest of the main fault plane concurrent with the northeast aftershock zone (Figure 8d). This far northwest aftershock structure is mainly defined by en echelon northeast striking conjugate to near-perpendicular structures that step to greater depth northwestward, away from the termination of activity related to the main fault zone.

5. Driving Mechanisms

The Mogul earthquake swarm illustrates the complexity of faulting and earthquake processes and the propensity of multiple types of faulting to occur in concert. This complexity may be characteristic of many Basin and Range sequences, but we rarely have similar high-density station coverage. The dense network coverage provided by temporary digital stations is essential to understanding the Mogul sequence. Excellent recording enables us to analyze spatiotemporal evolution in unprecedented detail using relocation and clustering. We now assess the spatiotemporal evolution of Mogul in the context of driving mechanisms.

Two principal driving mechanisms of seismic swarms are fluids and aseismic slip; they are often discriminated using migration patterns and rates, as well as association with direct observations of aseismic slip or fluid movement. For example, *Lohman and McGuire* [2007] interpret earthquake swarms as driven by aseismic creep in the Salton Trough, California, based on fast seismicity migration (~1 km/h) and geodetically observed deformation much larger than that explained by seismicity alone. *Chen and Shearer* [2013] also attributed fast migration rates over short time periods (~0.5 km/h over 2 h) to aseismic triggering processes in California foreshock sequences. On the other hand, microseismicity following fluid injection at the German Continental Deep Drilling Borehole [e.g., *Shapiro et al.*, 1997] and related to magmatic fluid circulation below Mount Rainier, Washington [e.g., *Shelly et al.*, 2013] migrated at much slower rates (~1 m^2/s) over longer time periods (days to weeks). When direct evidence is lacking, spatiotemporal migration rates and seismicity patterns have been used to distinguish between aseismic slip and fluid-related driving mechanisms [e.g., *Chen and Shearer*, 2011]. Because hot springs and geothermal activity are prevalent in western Nevada and eastern California [e.g., *Garside*, 1974], we begin by exploring pore pressure or fluid migration as a plausible driving force.

5.1. Evidence for Fluid as a Driving Mechanism

Lawton hot springs and the Truckee River in the area of the Mogul earthquakes (Figure 1c) could be a source of fluid that facilitated clustering of earthquakes in the foreshock period. Unfortunately, there were not sufficient enough measurements of fluids at Mogul to make an assessment on direct observation alone. We, therefore, rely on inferences from seismicity to identify fluid as a driving mechanism such as event migration, increased velocity ratios, and fault geometry.

5.1.1. Event Migration

To test for fluid diffusion, we model seismicity using the equation of *Shapiro et al*. [1997] by calculating the distance r of a propagating pore pressure front diffusing at rate D during time t through a homogeneous isotropic saturated poroelastic medium from a point source as

$$r = \sqrt{4\pi Dt}. \tag{3}$$

It describes a parabola-shaped distance envelope in which the migration rate is faster at the time of initial injection and slows away from the injection source. The model is based on a point source injection and requires generation of seismicity early in the process to isolate an earthquake diffusion triggering mechanism.

Starting from the locations of the first relocated earthquake, we estimate the hypocentral distance within which 95% of the earthquakes occur within using a moving window of 25 events each (black diamonds in Figures 9a and 9b). Although early activity is not very well fit by common fluid diffusion rates [e.g., *Duverger et al*., 2015], the 95% distance estimates later in the foreshock sequence very closely match a diffusion rate of 0.1 m^2/s (Figure 9a). We experiment with distance calculated from each of the first three events (located <500 m apart on the same day) and find that sequence migration is robust. The initial discrepancy could be because natural fluids do not initiate from a single point source, fluid pathways are very complex, or because sufficient locatable seismicity was not generated or detected early in the sequence. Temporary
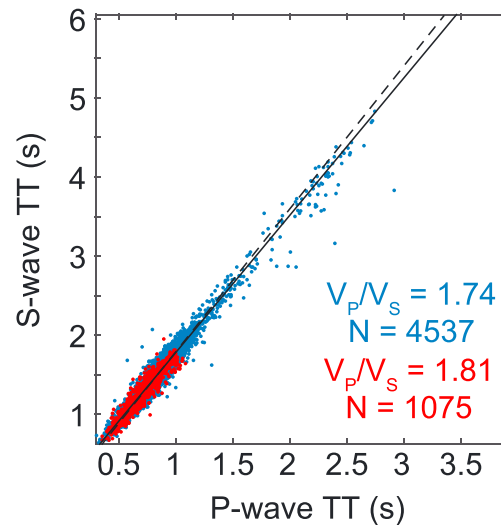
Figure 10. Graph of *P* wave travel time versus *S* wave travel time for 4537 arrivals recorded at distant stations using *P* wave travel times <10 s as a proxy for ~50 km radius (blue) and 1075 along-fault travel times recorded on near-source stations using *P* wave travel times <1 s as a proxy for ~5 km radius (red). Best fit lines are shown.

instruments deployed in early March, several weeks into the sequence, likely contribute to the more complete catalog and a better fit from 20–60 days into the sequence.

Regardless of the initial misfit, seismicity is spreading at a rate consistent with a diffusion model in the range of 0.1–0.25 m^2/s or at a constant migration on the order of tens of meters per day (Figure 9a). Migration rates on this order are associated with fluid flow through a fractured volume [e.g., *Parotidis et al.*, 2003; *Shelly et al.*, 2015]. In addition to the overall event migration from a point source, we observe spatial migration of earthquake clusters in the foreshock period that could be related to driving fluids. Weak downward migration of activity is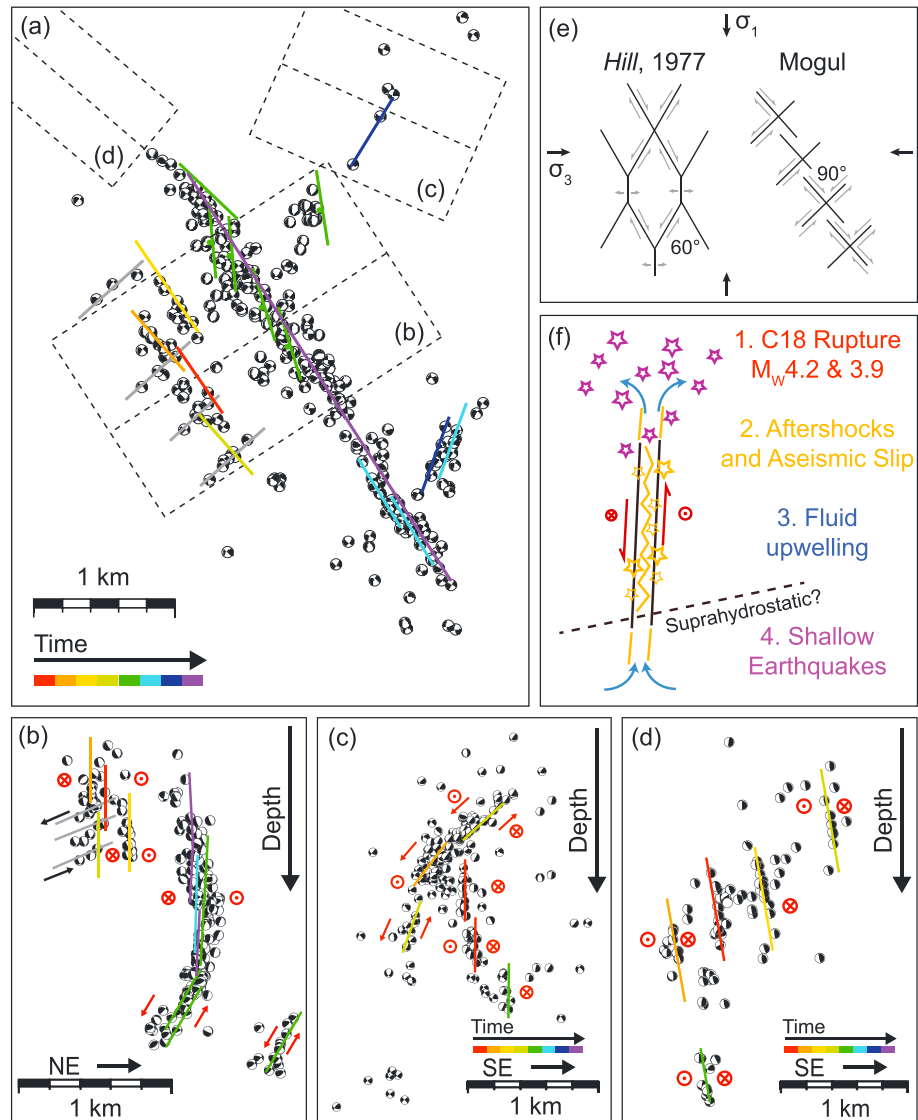 observed during the first foreshock phase (Figure 7a), while faster and more apparent downward migration is seen in the second foreshock phase (Figure 7b).

5.1.2. Fault-Valve Behavior

In addition to the downward migration of clusters discussed above, we also observe upward migration of clusters after the largest foreshock cluster, C18 (Figure 7e). *Shelly et al.* [2015] attributed upward migration of seismicity following an *M* 3.1 earthquake in the magmatic fluid-induced 2014 Mammoth Mountain swarm to "fault-valve" behavior. They hypothesized that the *M* 3.1 earthquake created permeable and dilatant pathways in the fault zone, providing a conduit for high-pressure fluid to rise from depth after the initial aftershock sequence. If this phenomenon is what we observe at Mogul, it suggests that cluster C18 ruptured into a suprahydrostatic fluid reservoir at very shallow depths (~5 km) in an area not associated with active magmatic or volcanic activity. Nearby Lawton hot springs and the Truckee River could explain fluid circulation and saturation at shallow depths (Figure 1c); however, there is no confirming evidence.

5.1.3. Increased Velocity Ratio

For an isotropic elastic medium, the slope of the best fit line of *P* wave travel times versus *S* wave travel times defines the V_P to V_S ratio. The wave equation suggests an empirical reference for V_P/V_S of 1.73 for intact, crystalline rock. *Wang et al.* [2012] showed that both saturation with an incompressible fluid (water) and crack density (anisotropy) affect the observed velocity ratio, with the latter strengthening the effect of the first. To explore the V_P/V_S ratio in the fault zone at Mogul, we compare the slope of arrival times of events away from the main fault zone at regional stations with that for earthquakes along the main fault zone at near-source stations (Figure 10). *P* wave travel times are used as a proxy for station distance. For the regional estimate, we use approximately 4500 arrivals from events with RMS values less than 0.02 s and *P* wave travel times less than 10 s, which is equivalent to an approximate station radius up to 50 km. For the near-fault estimate, we use the same event RMS cutoff with *P* wave travel times less than 1 s, resulting in 1075 arrival times. A *P* wave arrival time of 1 s corresponds to a radius of approximately 5 km. We determine the best fitting line using total least squares. The regional V_P/V_S ratio estimate is 1.74 ± 0.02 (standard error), while the slope of travel times at near-source stations is higher at 1.81 ± 0.003 (Figure 10). Comparing the two slopes in a *T* test suggests a very low probability that the two populations have the same slope; the difference is statistically significant.. The increased velocity ratio on near-source stations could support an interpretation of more fluids in the fault zone than in the surrounding region, although it may be related to increased fracture density resulting from damage around the largest events. We did not identify statistically significant temporal changes in V_P/V_S with the approach used here.

Figure 11. Sketch of fault kinematics of the Mogul 2008 earthquake swarm. (a) Map of 350 foreshock focal mechanisms with simplified faults colored by time. Gray lines represent fault structures highlighted by background activity over larger time periods. Dashed box labeled (b) denotes orientation of and mechanisms included in cross section (b). Focal mechanisms in vertical cross section are back-hemisphere. Red arrows show normal motion, arrow feather and bull's-eye symbols show into-the-paper and out-of-the-paper strike-slip motion, respectively. Black arrows show strike-slip motion parallel to the paper. (c, d) Cross sections of aftershock focal mechanisms (not shown in map view) matching cluster cross sections in Figures 8c and 8d. Kinematic symbols are the same as in Figure 11b. Fault lines are colored by relative timing of activity in each aftershock zone. (e) *Hill* [1977] mesh model for earthquake swarms (left) and model of Mogul early foreshock fault mesh (right). (f) Evolution of cluster C18 in terms of fault-valve behavior.

5.1.4. Fault-Fracture Mesh Geometry

The geometry and kinematics of foreshocks in the Mogul swarm (Figures 7 and 11a) reveal an organized network of short en echelon strike-slip faults (<500 m) activated by both clustered and background earthquakes. Foreshock cluster alignments suggest predominantly northwest striking right-lateral structures separated by a few hundred meters, whereas background earthquakes highlight left-lateral structures oriented at high angles (~85°) to northwest striking right-lateral faults (Figures 7a and 11b, and C1,). Crossing faults are aligned with the shear deformation direction estimated from GPS [*Hammond et al.*, 2011] and are oriented nearly 45° from the regional N-S oriented principal horizontal compressive stress inferred from regional strike-slip earthquakes [*Ruhl et al.*, 2016]. Additional en echelon shear faults are observed northeast of the main fault plane,

stepping downward and away from the main fault rupture (Figure 11d). Primarily, aftershock clusters and background earthquakes highlight these small, left-lateral faults (Figures 8d and 11d). The foreshock-defined fault-fracture mesh is offset to the west from the main shock fault zone by approximately 400 m (Figure 11). The mesh extends from ~2.5 km depth to 4 km depth and has a width of ~500 m. Seismicity is scattered above the mesh as shallow as ~1.5 km, with very few events locations above this depth.

Complex meshes of interconnecting shear and extensional faults have been observed in areas of magmatic activity [e.g., *Hill*, 1977] and in the step overs of major strike-slip faults [e.g., *Weaver and Hill*, 1978]. *Hill* [1977] originally proposed a model for earthquake swarms in which upwelling magmatic or hydrothermal fluids facilitate rupture on a mesh of interlinking minor shear faults and extensional fractures oriented perpendicular to the least compressive stress (Figure 11e). Our results are consistent with fault-fracture meshes commonly related to fluid-driven earthquake swarms in a variety of tectonic settings [*Sibson*, 1996], although failure planes are at higher angles (e.g., ~45°) to the most compressive stress than expected (Figure 11e). This suggests either very low friction and/or failure on preexisting faults. Alternatively, fault-perpendicular structures could represent tension fractures developed as a result of coseismic and aseismic shear slip. Although the Mogul area is heavily overprinted by Quaternary, Tertiary, and older structures, there are no mapped surface faults that correlate with the detailed deformation fabric resolved here (Figure 1). Results show that individual faults are activated transiently, but over the entire duration of the swarm define the aggregate fault-fracture mesh. If the mesh geometry defined by seismicity is controlled primarily by fluid flow, then the long duration of the sequence indicates long-term high fluid pressure in the shallow subsurface (for up to several months).

5.2. Evidence for Aseismic Slip

The total seismic moment modeled using InSAR by *Bell et al.* [2012] is approximately twice that of the cumulative moment of the main shock and all $M_w \geq 3.0$ events. This suggests significant aseismic slip, two thirds of which occurred prior to the 28 May InSAR scene (sequence day 94 in Figure 9). *Bell et al.* [2012] suggest that the aseismic slip is primarily postseismic; however, timing of interferogram pairs does not provide resolution required to detect aseismic slip very close in time to the main shock. For instance, Cluster C18, the largest and most energetic foreshock cluster, occurred within 2 days of the main shock. The rate and behavior of background seismicity following cluster C18 is anomalous in that it exhibits a clear migration pattern away from C18 (Figures 9d and S3). Cluster C18 impulsively reaches the full spatial extent expected for an M_w 4.1 earthquake assuming a stress drop of 3 MPa before background seismicity propagates away from the main shock hypocenter (Figure S3). The seismicity propagation rate is approximately 1 km/h over a 2–3 h time period (Figure 9d). This rate is consistent with migration of seismicity driven by aseismic slip [e.g., *Lohman and McGuire*, 2007; *Chen and Shearer*, 2013]. From InSAR, *Bell et al.* [2012] modeled the postseismic slip as equivalent to an M_w 5.0 earthquake; however, they do not resolve any aseismic slip in the foreshock period. Limitations in data collection (e.g., InSAR satellite image timing) may mask the presence of slow slip in the days prior to the main shock. Another possible explanation for the lack of surface geodetic evidence for aseismic slip in the foreshock period could be that aseismic slip after C18 propagated primarily to greater depths. The M_w 4.9 main shock is one of the smallest earthquakes in the Basin and Range to be modeled using InSAR, due likely to its extremely shallow depth [*Bell et al.*, 2012]. Perhaps preseismic slip, if present, was too deep and/or too small to be measured at the surface.

6. Conclusions

Detailed high-precision relocations of the Mogul earthquake swarm are highly organized in space and time and reveal details of fault zone geometry and seismicity that were previously unknown. Our new application of statistical clustering quantitatively and efficiently isolates spatiotemporal clusters previously isolated by tedious manual inspection. We interpret the Mogul swarm as "fluid driven" based on observations of event migration, fault-fracture mesh geometry, and fault-valve behavior. Seismicity spreads with an average velocity near 30 m/d and/or a diffusivity of 0.25 m²/s, consistent with fluid-driven migration rates from previous studies. Foreshocks also define a fault-fracture mesh consistent with previous studies of fluid-driven earthquake swarms. Background seismicity concurrent with the largest foreshock cluster C18 migrates away from the main shock at ~1 km/h, a rate consistent with seismicity migration velocities seen in swarms associated with aseismic slip. Seismicity clusters migrated upward following C18 consistent with fault-valve behavior in a saturated medium.

References

Allam, A. A., Y. Ben-Zion, I. Kurzon, and F. Vernon (2014), Seismic velocity structure in the Hot Springs and Trifurcation areas of the San Jacinto fault zone, California, from double-difference tomography, *Geophys. J. Int.*, *198*, 978–999, doi:10.1093/gji/ggu176.

Allen, J. L. (2005), A multi-kilometer pseudotachylyte system as an exhumed record of earthquake rupture geometry at hypocentral depths (Colorado, USA), *Tectonophysics*, *402*(1–4), 37–54, doi:10.1016/j.tecto.2004.10.017.

Anderson, J. G., I. Tibuleac, A. Anooshehpoor, G. Biasi, K. Smith, and D. von Seggern (2009), Exceptional ground motions recorded during the 26 April 2008 M_w 5.0 earthquake in Mogul, Nevada, *Bull. Seismol. Soc. Am.*, *99*(6), 3475–3486, doi:10.1785/0120080352.

Anderson, J. G., and K. Nanjo (2013), Distribution of earthquake cluster sizes in the western United States and in Japan, *Bull. Seism. Soc. Am.*, *103*(1), pp. 412–423, doi:10.1785/0120100212.

Antonioli, A., D. Piccinini, L. Chiaraluce, and M. Cocco (2005), Fluid flow and seismicity pattern: Evidence from the 1997 Umbria-Marche (central Italy) seismic Sequence, *Geophys. Res. Lett.*, *32*, L10311, doi:10.1029/2004GL022256.

Bell, J. W., and L. J. Garside (1987), *Verdi Quadrangle: Geologic Map*, Nev. Bur. of Mines and Geol., Univ. of Nev., Reno.

Bell, J. W., F. Amelung, and C. D. Henry (2012), InSAR analysis of the 2008 Reno-Mogul earthquake swarm: Evidence for westward migration of Walker Lane style dextral faulting, *Geophys. Res. Lett.*, *39*, L18306, doi:10.1029/2012GL052795.

Cashman, P. H., J. H. Trexler Jr., M. C. Widmer, and S. J. Queen (2012), Post-2.6 Ma tectonic and topographic evolution of the northeastern Sierra Nevada: The record in the Reno and Verdi basins, *Geosphere*, *8*(5), 972–990, doi:10.1130/GES00764.1.

Chen, X., and P. M. Shearer (2011), Comprehensive analysis of earthquake source spectra and swarms in the Salton Trough, California, *J. Geophys. Res.*, *116*, B09309, doi:10.1029/2011JB008263.

Chen, X., and P. M. Shearer (2013), California foreshock sequences suggest aseismic triggering process, *Geophys. Res. Lett.*, *40*, 2602–2607, doi:10.1002/grl.50444.

Chen, X., P. M. Shearer, and R. E. Abercrombie (2012), Spatial migration of earthquakes within seismic clusters in Southern California: Evidence for fluid diffusion, *J. Geophys. Res.*, *117*, B04301, doi:10.1029/2011JB008973.

Chester, F. M., J. P. Evans, and R. L. Biegel (1993), Internal structure and weakening mechanisms of the San Andreas fault, *J. Geophys. Res.*, *98*, 771–786, doi:10.1029/92JB01866.

dePolo, C. M., J. G. Anderson, D. M. dePolo, and J. G. Price (1997), Earthquake occurrence in the Reno-Carson City urban corridor, *Seismol. Res. Lett.*, *68*, 401–412.

Duverger, C., M. Godano, P. Bernard, H. Lyon-Caen, and S. Lambotte (2015), The 2003–2004 seismic swarm in the western Corinth rift: Evidence for a multiscale pore pressure diffusion process along a permeable fault system, *Geophys. Res. Lett.*, *42*, 7374–7382, doi:10.1002/2015GL065298.

Eshelby, J. D. (1957), The determination of the elastic field of an ellipsoidal inclusion and related problems, *Proc. R. Soc. London A*, *241*, 376–396.

Finzi, Y., E. H. Hearn, Y. Ben-Zion, and V. Lyakhovsky (2009), Structural properties and deformation patterns of evolving strike-slip faults: Numerical simulations incorporating damage rheology, *Pure Appl. Geophys.*, *166*, 1537–1573, doi:10.1007/s00024-009-0522-1.

Garside, L. J. (1974), Geothermal exploration and development in Nevada through 1973, *Rep. 21*, Nev. Bur. of Mines and Geol.

Gu, C., A. Y. Schumann, M. Baiesi, and J. Davidsen (2013), Triggering cascades and statistical properties of aftershocks, *J. Geophys. Res. Solid Earth*, *118*, 4278–4295, doi:10.1002/jgrb.50306.

Hainzl, S. (2004), Seismicity patterns of earthquake swarms due to fluid intrusion and stress triggering, *Geophys. J. Int.*, *159*, 1090–1096, doi:10.1111/j.1365-246X.2004.02463.x.

Hainzl, S., and T. Fischer (2002), Indication for a successively triggered rupture growth underlying the 2000 earthquake swarm in Vogtland/NW Bohemia, *J. Geophys. Res.*, *107*(B12), 2338, doi:10.1029/2002JB001865.

Hammond, W. C., and W. Thatcher (2007), Crustal deformation across the Sierra Nevada, northern Walker Lane, basin and range transition, western United States measured with GPS, 2000–2004, *J. Geophys. Res.*, *112*, B05411, doi:10.1029/2006JB004625.

Hammond, W. C., G. Blewitt, and C. Kreemer (2011), Block modeling of crustal deformation of the northern Walker Lane and Basin and Range from GPS velocities, *J. Geophys. Res.*, *116*(B04402), doi:10.1029/2010JB007817.

Hardebeck, J. L., and P. M. Shearer (2002), A new method for determining first-motion focal mechanisms, *Bull. Seismol. Soc. Am.*, *92*, 2264–2276.

Hill, D. P. (1977), A model for earthquake swarms, *J. Geophys. Res.*, *82*, 1347–1352, doi:10.1029/JB082i008p01347.

Ibs-von Seht, M., T. Plenefisch, and K. Kinge (2008), Earthquake swarms in continental rifts—A comparison of selected cases in America, Africa, and Europe, *Tectonophysics*, *452*, 66–77, doi:10.1016/j.tecto.2008.02.008.

Ichinose, G. A., K. D. Smith, and J. G. Anderson (1998), Moment tensor solutions of the 1994 to 1996 Double Spring Flat, Nevada, earthquake sequence and implications for local tectonic models, *Bull. Seismol. Soc. Am.*, *88*(6), 1363–1378.

Ichinose, G. A., J. G. Anderson, K. D. Smith, and Y. Zeng (2003), Source parameters of eastern California and western Nevada earthquakes from regional moment tensor inversion, *Bull. Seismol. Soc. Am.*, *93*(1), 61–84, doi:10.1785/0120020063.

Klein, F. W. (1978), Hypocenter locations program HYPOINVERSE, U.S. Dep. of the Inter., Geol. Surv.

Lohman, R. B., and J. J. McGuire (2007), Earthquake swarms driven by aseismic creep in the Salton Trough, California, *J. Geophys. Res.*, *112*, B04405, doi:10.1029/2008JB004596.

Mogi, K. (1963), Some discussions on aftershocks, foreshocks, and earthquake swarms: The fracture of a semi-infinite body caused by an inner stress origin and its relation to the earthquake phenomenon (third paper), *Bull. Earthquake Res. Inst.*, *41*, 615–658.

Pacchiani, F., and H. Lyon-Caen (2010), Geometry and spatio-temporal evolution of the 2001 Agios Ioanis earthquake swarm (Corinth Rift, Greece), *Geophys. J. Int.*, *180*, 59–72, doi:10.1111/j.1365-246X.2009.04409.x.

Parotidis, M., E. Rothert, and S. A. Shapiro (2003), Pore-pressure diffusion: A possible triggering mechanism for the earthquake swarms 2000 in Vogtland/NW-Bohemia, central Europe, *Geophys. Res. Lett.*, *30*(20), 2075, doi:10.1029/2003GL018110.

Ruhl, C., S. L. Bilek, and J. Stankova-Pursley (2010), Relocation and characterization of the August 2009 microearthquake swarm above the Socorro magma body in the central Rio Grande Rift, *Geophys. Res. Lett.*, *37*, L23304, doi:10.1029/2010GL045162.

Ruhl, C. J., T. C. Seaman, K. D. Smith, and G. M. Kent (2016), Seismotectonic and seismic hazard implications for the Reno-Tahoe area of the Walker Lane in Nevada and California, in *AEG Special Volume on Applied Geology in California*, pp. 879–895, Star Publishing Co. Inc., Redwood, Calif.

Schaff, D. P., G. H. R. Bokelmann, G. C. Beroza, F. Waldhauser, and W. L. Ellsworth (2002), High-resolution image of Calaveras Fault seismicity, *J. Geophys. Res.*, *107*(B9), 2186, doi:10.1029/2001JB000633.

Shapiro, S. A., E. Huenges, and G. Borm (1997), Estimating the crust permeability from fluid-injection-induced seismic emission at the KTB site, *Geophys. J. Int.*, *131*, F15–F18.

Shelly, D. R., S. C. Moran, and W. A. Thelen (2013), Evidence for fluid-triggered slip in the 2009 Mount Rainier, Washington earthquake swarm, *Geophys. Res. Lett.*, *40*, 1506–1512, doi:10.1002/grl.50354.

Shelly, D. R., T. Taira, S. G. Prejean, D. P. Hill, and D. S. Dreger (2015), Fluid-faulting interactions: Fracture-mesh and fault-valve behavior in the February 2014 Mammoth Mountain, California, earthquake swarm, *Geophys. Res. Lett.*, *42*, 5803–5812, doi:10.1002/2015GL064325.

Shevenell, L. (2016), Lawton Hot Springs Facility, Nevada. [Available at http://repository.stategeothermaldata.org/repository/resource/3592f7bc37ea27adea06455fbf378278/, Retrieved 9 March 2016.]

Shimojo, K., B. Enescu, Y. Yagi, and T. Takeda (2014), Fluid-driven seismicity activation in northern Nagano region after the 2011 *M*9.0 Tohoku-oki earthquake, *Geophys. Res. Lett.*, *41*, 7524–7531, doi:10.1002/2014GL061763.

Sibson, R. H. (1996), Structural permeability of fluid-driven fault-fracture meshes, *J. Struct. Geol.*, *18*(8), 1031–1042.

Smith, K. D., D. von Seggern, D. dePolo, J. Anderson, G. Biasi, and R. Anooshehpoor (2008), Seismicity of the 2008 Mogul-Somersett west Reno, Nevada, earthquake sequence, *Eos Trans. AGU*, *89*(53), Abstract S53C-02.

Smith, K. D., D. von Seggern, and J. G. Anderson (2010), Foreshock sequence of the 2008 *M*w 5.0 Mogul-Somersett, Nevada Earthquake, poster presented at the SSA Annual Meeting, 20–23 April, Portland, Oreg.

Spicak, A., and J. Horalek (2001), Possible role of fluids in the process of earthquake swarm generation in the West Bohemia/Vogtland seismoactive region, *Tectonophysics*, *336*, 151–161.

Stewart, J. H. (1988), Tectonics of the Walker Lane Belt, Western Great Basin: Mesozoic and Cenozoic deformation in a zone of shear, in *Metamorphism and Crustal Evolution of the Western United States*, vol. 7, pp. 683–713, Englewood Cliff, Prentice-Hall, N. J.

Surpless, B. (2008), Modern strain localization in the central Walker Lane, western United States: Implications for the evolution of intraplate deformation in transtensional settings, *Tectonophysics*, *457*, pp. 239–253.

Sykes, L. R. (1970), Earthquake swarms and sea-floor spreading, *J. Geophys. Res.*, *75*, 6598–6611, doi:10.1029/JB075i032p06598.

U.S. Geological Survey and Nevada Bureau of Mines and Geology (2006), Quaternary fault and fold database for the United States, USGS. [Available at http://earthquakes.usgs.gov/regional/qfaults/, accessed November 14, 2012.]

Unsworth, M. J., P. E. Malin, G. D. Egbert, and J. R. Booker (1997), Internal structure of the San Andreas fault at Parkfield, California, *Geology*, *25*(4), 359–362.

Utsu, T. (1961), A statistical study on the occurrence of aftershocks, *Geophys. Mag.*, *30*, 521–605.

Valoroso, L., L. Chiaraluce, and C. Collettini (2014), Earthquakes and fault zone structure, *Geology*, *42*(4), 343–346, doi:10.1130/G35071.1.

Vidale, J. E., and P. M. Shearer (2006), A survey of 71 earthquake bursts across southern California: Exploring the role of pore fluid pressure fluctuations and aseismic slip as drivers, *J. Geophys. Res.*, *111*, B05312, doi:10.1029/2005JB004034.

von Seggern, D. H., J. G. Anderson, I. M. Tibuleac, and G. P. Biasi (2015), Double-difference location and ground-truth classification of the 2008 Mogul, Nevada, very shallow earthquake sequence, *Seismol. Res. Lett.*, *86*(1), 1–12.

Waite, G. P., and R. B. Smith (2002), Seismic evidence for fluid migration accompanying subsidence of the Yellowstone caldera, *J. Geophys. Res.*, *107*(B9), 2177, doi:10.1029/2001JB000586.

Waldhauser, F., and W. L. Ellsworth (2000), A double-difference earthquake location algorithm: Method and application to the northern Hayward fault, California, *Bull. Seismol. Soc. Am.*, *90*(6), 1353–1368.

Waldhauser, F., W. L. Ellsworth, D. P. Schaff, and A. Cole (2004), Streaks, multiplets, and holes: High-resolution spatio-temporal behavior of Parkfield seismicity, *Geophys. Res. Lett.*, *31*, L18608, doi:10.1029/2004GL020649.

Wang, X. Q., A. Schubnel, J. Fortin, E. C. David, Y. Gueguen, and H. K. Ge (2012), High V_p/V_s ratio: Saturated cracks or anisotropy effects? *Geophys. Res. Lett.*, *39*, L11307, doi:10.1029/2012GL051742.

Weaver, C. S., and D. P. Hill (1978), Earthquake swarms and local crustal spreading along major strike-slip faults in California, *Pure Appl. Geophys.*, *117*, 51–64.

Wiemer, S. (2001), A software package to analyze seismicity: ZMAP, *Seismol. Res. Lett.*, *72*(2), 374–383.

Wesnousky, S. G., J. M. Bormann, C. Kreemer, W. C. Hammond, and J. N. Brune (2012), Neotectonics, geodesy, and seismic hazard in the Northern Walker Lane of Western North America: Thirty kilometers of crustal shear and no strike-slip? *Earth Planet. Sci. Lett.*, *329*, 133–140.

Zaliapin, I., and Y. Ben-Zion (2013a), Earthquake clusters in southern California I: Identification and stability, *J. Geophys. Res. Solid Earth*, *118*, 2847–2864, doi:10.1002/jgrb.50179.

Zaliapin, I., and Y. Ben-Zion (2013b), Earthquake clusters in southern California II: Classification and relation to physical properties of the crust, *J. Geophys. Res. Solid Earth*, *118*, 2865–2877, doi:10.1002/jgrb.50178.

Zaliapin, I., and Y. Ben-Zion (2015), Artefacts of earthquake location errors and short-term incompleteness on seismicity clusters in southern California, *Geophys. J. Int.*, *202*(3), 1949–1968.

Zaliapin, I., A. Gabrielov, V. Keilis-Borok, and H. Wong (2008), Clustering analysis of seismicity and aftershock identification, *Phys. Rev. Lett.*, *101*, 018501.

Zhang, Q., and P. M. Shearer (2016), A new method to identify earthquake swarms applied to seismicity near the San Jacinto Fault, California, *Geophys. J. Int.*, *205*(2), 995–1005.

Zoback, M., S. Hickman, and W. Ellsworth (2010), Scientific drilling into the San Andreas fault, *Eos Trans. AGU*, *91*(22), 197–204, doi:10.1029/2010EO220001.